JGR Atmospheres

RESEARCH ARTICLE
10.1029/2024JD041804

Observation of Gravity Waves Generated by Convection and the "Moving Mountain" Mechanism During Stratéole-2 Campaigns and Their Impact on the QBO

Milena Corcos[1], Martina Bramberger[2], M. Joan Alexander[1], Albert Hertzog[3], Chuntao Liu[4], and Corwin Wright[5]

[1]NorthWest Research Associates, Boulder, CO, USA, [2]Now at National Center for Atmospheric Research, Boulder, CO, USA, [3]Laboratoire de Météorologie Dynamique, École Polytechnique, Sorbonne Université, Palaiseau, France, [4]Texas A&M Corpus Christi, Houston, TX, USA, [5]Bath University, Bath, UK

Key Points:

- Momentum fluxes, ground-based, and intrinsic phase speeds are derived from balloon observations
- Convective gravity waves from the moving mountain mechanism occur 5% of the time and are concentrated in phase speeds lower than 15 m/s
- Despite their infrequent occurrence, they play an outsized role in driving the quasi biennial oscillation below 50 hPa

Correspondence to:

M. Corcos,
milena@nwra.com

Citation:

Corcos, M., Bramberger, M., Alexander, M. J., Hertzog, A., Liu, C., & Wright, C. (2025). Observation of gravity waves generated by convection and the "moving mountain" mechanism during stratéole-2 campaigns and their impact on the QBO. *Journal of Geophysical Research: Atmospheres*, *130*, e2024JD041804. https://doi.org/10.1029/2024JD041804

Received 15 JUL 2024
Accepted 1 MAR 2025

Author Contributions:

Conceptualization: Milena Corcos, Martina Bramberger
Data curation: Chuntao Liu
Formal analysis: Milena Corcos
Funding acquisition: Martina Bramberger
Investigation: Milena Corcos, M. Joan Alexander
Methodology: Milena Corcos, Martina Bramberger
Project administration: Martina Bramberger
Resources: Martina Bramberger, Chuntao Liu
Software: Milena Corcos, Albert Hertzog, Corwin Wright
Supervision: M. Joan Alexander
Validation: Milena Corcos, Martina Bramberger
Visualization: Milena Corcos

Abstract Convective gravity waves are important for the forcing of the quasi biennial oscillation (QBO). There is a wave component that is stationary with respect to the convective cells that is triggered by convection acting like a barrier to the background flow (moving mountain mechanism). Waves from this mechanism have only been observed in a few case studies and are not parameterized in climate models. However, the representation of the whole spectrum of gravity waves is crucial for the simulation of the QBO, especially in the lowermost stratosphere (below 50 hPa) where the QBO amplitudes are under-estimated in current global circulation models. In this study, we present analysis of convective gravity wave observations from superpressure balloons in boreal winter 2019 and 2021, retrieving phase speeds, momentum fluxes, and drag. We also identify waves generated by the moving mountain mechanism using the theory of the Beres scheme as a basis. These waves do not have a specific period, but are of smaller horizontal scale, on average around 300 km, which is similar to the scale of convective systems. Our results show that gravity waves contribute up to 2/3 to the QBO forcing below 50 hPa and waves from the moving mountain mechanism are responsible for up to 10% of this forcing.

Plain Language Summary Convective rain cells in the tropics are known to generate waves that drive global atmospheric circulation patterns in the tropical stratosphere. One mechanism of wave generation is called a "moving mountain" mechanism. In this mechanism, the convective rain cell acts as a mountain-like obstacle to the ambient wind, which generates waves that are stationary with respect to the convective rain cell. In our study, we determine the impact of this type of wave from super-pressure balloon observations. We find that although these waves do not occur often in our observations, they are of bigger amplitude and play an outsized role in driving the tropical stratospheric winds.

1. Introduction

The quasi-biennial oscillation (QBO) in equatorial lower-stratospheric zonal mean winds is a prominent feature where alternating easterly and westerly zonal mean wind zones descend from about 10 hPa to 100 hPa with an average period of about 28 months. In principal, the QBO is driven by the interaction of tropical Kelvin, mixed-Rossby-gravity, inertia-gravity and small-scale gravity waves, with the mean flow (Baldwin et al., 2001). Current evidence suggests that gravity waves contribute from 50% to 75% of the forcing, depending on the phase of the QBO. Therefore, the representation and parameterization of gravity waves, mostly generated by convection in the tropics (Convectively generated Gravity Waves, or CGWs) is crucial for the simulation of the QBO, especially in the lowermost stratosphere (below 50 hPa) where the amplitudes are under-estimated in current global circulation models (GCMs) (Anstey et al., 2022).

Together with planetary-scale Kelvin waves, the breaking and dissipation of tropical gravity waves in the stratosphere drives the descent of QBO zonal wind changes. Breaking of these waves occurs when they become unstable, which is more likely as they approach a critical level, where their ground-based phase speed c equals the wind speed in their propagation direction. That way, c together with propagation direction has a first order control on when and where gravity waves break and impart a drag force on the circulation. For now, these CGWs are not explicitly resolved in global climate models and their interaction with the surrounding flow, in particular their drag, is included using parameterizations.

Writing – original draft: Milena Corcos, Martina Bramberger, M. Joan Alexander
Writing – review & editing: Milena Corcos, M. Joan Alexander, Albert Hertzog

The current CGW Beres parameterization scheme (Beres et al., 2005) implemented in the Whole Atmosphere Community Climate Model (WACCM) launches waves at 1° × 1° grid locations when convection is active. In this parameterization, CGWs are assumed to be launched at the top of convective rain cells, whenever they occur in the model, and it is also assumed that the convective latent heating is concentrated only in a minor 5% of the GCM grid-cell area. In this scheme, a spectrum of CGWs are generated by an oscillating heat source, and their c spectrum is also tied to the vertical profile of latent heating and the mean wind in the convective heating layer. The momentum flux is directly proportional to the square of the maximum heating rate. The waves are assumed to propagate forward and backward in the plane defined by the vector motion of the convective cell, which is assumed to be the 700 hPa wind vector. Note, this CGW Beres parameterization scheme currently only takes into account the nonstationary CGWs generated by an oscillating heat source (Beres et al., 2005; Richter et al., 2010). We define here "stationary" or "non-stationary" waves as relative to their sources. Thus, stationary waves phase speed is not null but close to the motion of their source. This terminology will be used moving forward in our paper. The nonstationary waves are necessary for simulating the QBO because they fill a broad spectrum of phase speeds, yet both observations and simulations suggest that stationary CGWs have much larger amplitudes and represent an important gap in the spectrum at low phase speeds (Alexander et al., 2006, 2021).

The stationary CGWs are generated by the obstacle or "moving mountain" effect, where the convective cell acts as an obstacle to the surrounding flow (Beres et al., 2004; Clark et al., 1986; Pfister et al., 1993). Pfister et al. (1993) and Beres et al. (2004) modeled this effect as a linear response to the steady component of convective heating when there is a non zero background flow relative to the cell motion. This generates vertically propagating gravity waves with upstream-tilted phase fronts, similar to a wave generated by a mountain, and these waves are modeled as stationary relative to the convective cell. For a propagating cell, their ground-based phase speed equals the convective cell propagation speed, and their direction is given by the vector difference of the cell motion and the wind at the top of the cell. As the propagation of tropical convective cells rarely exceeds 15 m/s, momentum fluxes associated with these waves are concentrated at lower phase speeds (Clark et al., 1986). For now, due to their small scale, their intermittent occurrence, and the lack of observations of their momentum fluxes (a key variable in the current parameterizations), it has been difficult to constrain their effects in atmospheric circulation models.

In this study we present analysis of convective gravity wave observations from superpressure balloons over boreal winters 2019 and 2021 in terms of phase speeds, momentum flux, and drag. This analysis can be used to constrain CGW parameterizations, and we provide a special focus here on the stationary component of these waves. The second section of this paper is dedicated to present the balloon observations as well as our method of data analysis. The third section describes first the characteristics of gravity waves associated with the moving mountain mechanism, then distinguishes these characteristics in different regions of the tropical band. Finally, the discussion and conclusions focus on the inter annual variability of convective gravity wave drag and the contribution of the stationary component to the zonal flux and QBO drive.

2. Data and Methods

2.1. Stratéole-2 Observations

Stratéole-2 is a series of balloon campaigns in the deep tropics aimed at studying climate processes in the tropical tropopause layer (TTL) in several different years and phases of the QBO. A unique aspect of this campaign comes from the use of superpressure balloons, advected by the wind, that act as quasi-Lagrangian tracers. Two campaigns (named hereafter as C0 and C1) occurred, respectively in boreal winters 2019 (from 2019/11/11 to 2020/02/22) and 2021 (from 2021/10/19 to 2022/01/25), and at two slightly different phases of the QBO. During these campaigns, 8 and 17 balloons were respectively launched from Mahé, a Seychelles island (55.52° E, 4.67° S), and balloons flew for up to 3 months each.

The first campaign is described in Corcos et al. (2021). Table 1 summarizes the flight characteristics of the second campaign. Two types of balloons were launched, "TTL" and "STR" types with equilibrium altitudes of approximately 18 and 20 km, respectively. Both are globally almost equally represented during the two campaigns. Each balloon carries a gondola with a GPS receiver and a Tsen (Thermodynamic sensor) instrument, which measures the air pressure and temperature. Both have a time resolution of 30 s, which in theory enables sampling of the full period spectrum of atmospheric waves in the lower stratosphere.

Table 1
Characteristics of 2021 Stratéole-2 C1 Balloon Flights

Flight	Altitude (km)	Pressure (hPa)	Launch (UT)	End (UT)	Duration (day)
01_TTL5	18.4	73.6	2021-10-19	2021-10-21	1
02_STR1	20.2	55.1	2021-10-20	2021-11-01	12
03_TTL4	18.5	72.1	2021-10-20	2021-11-21	31
04_STR2	20.1	55.6	2021-10-20	2021-11-19	30
05_TTL3	18.5	72.8	2021-10-27	2021-12-17	50
06_TTL5	18.6	72.6	2021-10-28	2021-12-11	43
07_TTL4	18.5	72.5	2021-11-01	2021-12-16	44
08_STR1	20.3	53.3	2021-11-04	2021-12-29	54
09_STR2	20.2	54.0	2021-11-05	2022-01-12	67
10_TTL3	18.6	71.7	2021-11-08	2021-12-16	38
11_TTL1	18.6	72.1	2021-11-08	2021-12-15	37
12_STR4	20.5	52.2	2021-11-12	2022-01-02	51
13_STR1	20.4	52.7	2021-11-15	2022-01-25	71
15_TTL4	18.6	70.9	2021-11-12	2022-01-02	56
16_TTL5	18.5	72.6	2021-11-22	2021-12-19	26
17_TTL3	18.5	72.3	2021-11-25	2021-12-16	20
Total days					631

Figure 1 illustrates an overview of the original 30 s time resolution observations during both campaigns. All balloons were released in the QBO, flying eastward for the most part, and observations were mostly gathered within 15° of the equator, circling the whole tropical band. During C0, the QBO was westerly at balloon floating levels with easterlies above, whereas in C1 the zero wind line had descended to the balloon floating levels ("TTL" and "STR"). Although the balloons are overall globally well distributed, many stalled over convective systems in the Maritime Continent, which explains the higher number of observations in that region during both campaigns. The background QBO wind shear was negative during both campaigns but weaker in C1 (3.4 and 1.3 m/s/km, for C0 and C1, respectively, based on balloon observations), some balloons even reversed direction from eastward to westward, which partially explains the lack of observations over the Atlantic ocean during that campaign and the higher number of observations above the eastern Pacific ocean during C1. Finally, C1 also differs from C0 by the shorter flights (table 1) associated with balloon issues.

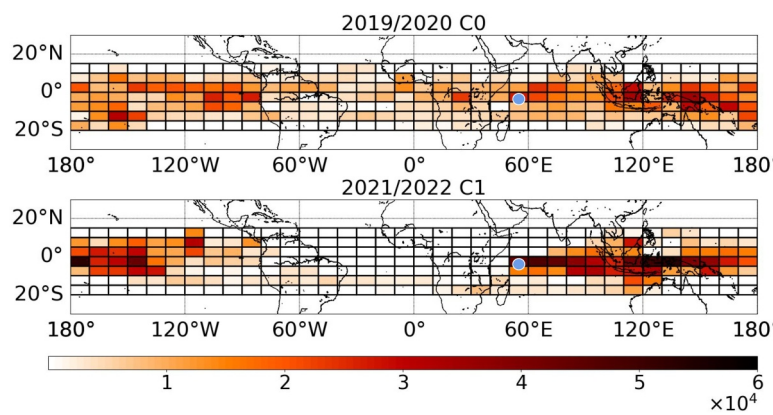

Figure 1. Number of 30 s observations of the two first campaigns (C0 top and C1 bottom) of Stratéole-2. The blue dot represents the balloon launching site.

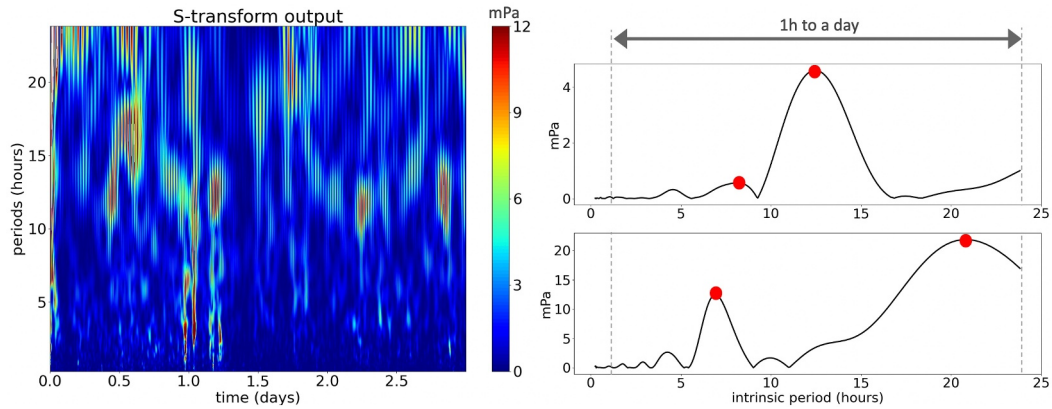

Figure 2. Left panel: S transform of momentum flux on a 4 days sample. Right panel: examples of momentum flux amplitude as a function of wave period at two random times. The centers of the two largest amplitude wave packets are spotted with a red dot.

2.2. Derivation of Gravity Wave Properties: Momentum Fluxes, Intrinsic and Ground-Based Phase Speeds

To retrieve the momentum fluxes and phase speeds from the balloon observations we follow the method described in Boccara et al. (2008) and Vincent and Hertzog (2014).

The zonal and meridional components of the wind are inferred from the balloon consecutive positions, with a precision of $\sim$0.1 m/s (Podglajen et al., 2014). As in Corcos et al. (2021), the balloon's vertical displacements (ζ') are derived from the pressure observations, assuming hydrostaticity and a perfect isopycnic behavior of the balloon (Podglajen et al., 2016). This assumption is realistic for wave-induced disturbances with intrinsic periods longer than twice the Brunt-Väisälä period ($2\pi/N$). In this range of frequencies, the air-parcel and balloon vertical displacements are linearly related by a constant coefficient that enables us to transform the isopycnic motion of the balloons to the air parcel isentropic vertical motion (Podglajen et al., 2014).

Balloon timeseries are processed using an S transform (Bramberger et al., 2022; Stockwell et al., 1996), which gives a time-frequency representation of the signal with a frequency dependent resolution. We include wave periods in the range in 1–24 hr, a choice further explained by the need for wave packet selections in the next paragraph. This range in frequencies also avoids concerns with either the balloon neutral oscillations at their equilibrium density level (which occur at $\hat{\omega}_b \lesssim N$), or the balloon tendency to depart from a perfect isopycnic behavior at frequencies near N. The S transform method applied to quasi-Lagrangian balloon measurements provides information in the time/intrinsic-frequency space that enables us to retrieve properties of individual wave packets.

We define a wave packet as a local amplitude maximum in wave period at each time (several wave packets can be distinguished at each time step), and only the center of each wave packet is used to derive the detailed wave properties. In that regard, our method differs from Corcos et al. (2021) and Podglajen et al. (2016) who integrated the wave momentum fluxes over the full range of frequencies and did not compute phase speeds or individual packet properties. Figure 2 illustrates wave packet identification from the S-transform. Wave packets are associated with a specific intrinsic period and are separated by a local minimum of amplitude. A wave packet's intrinsic phase speed is indeed only well-defined at the peak and tends toward infinity at the edge of peaks. As illustrated in the figure, local maxima in the time/frequency plot can sometimes evolve in time, but here our definition of wave packet treats identified maxima at each time as independent wave packets, which is necessary to compute phase speeds and other properties, and which allows these properties to evolve in time as observed. Approximately, 76,000 wave packets can be retrieved per campaign in the period range of 1 hr to a day. We analyze each wave packet separately to obtain momentum fluxes $\overline{\rho u' w'}(t, \hat{\omega})$ and intrinsic phase speeds $\hat{c}(t, \hat{\omega})$, where $\overline{\rho}$ is the flight-averaged balloon density. As in Boccara et al. (2008), the gravity-wave polarization relations (Fritts & Alexander, 2003) (their equation 27) is also used to infer the local wave direction of propagation θ, relative to the East. It is defined as $\vec{k}/|\vec{k}|$. Then, using the polarization relation between w' and $u'_{\parallel}$, we follow Boccara et al. (2008) to obtain the momentum fluxes:

$$\Re\left(w' u'^{*}_{\parallel}\right) = -\frac{\hat{\omega}}{\bar{\rho} H N^2} \Im\left(p'_l u'^{*}_{\parallel}\right) \quad (1)$$

with H the density scale height, p'_l is the Lagrangian pressure perturbation, $u'^{*}_{\parallel}$ is the horizontal motion parallel to the direction of propagation θ, $\Re$ and $\Im$ stands for the real and imaginary part, respectively. Note here that we only retain the real part of the equation as the Imaginary part vanishes when averaged over a wave period Boccara et al. (2008). Finally, we present density weighted momentum fluxes as they would be independent of the altitude if waves do not break (Vincent & Alexander, 2000). Density is well defined as balloons are flying on constant density levels. Intrinsic phase speeds $\hat{c}$ are calculated following Boccara et al. (2008):

$$\hat{c} = \frac{2}{\bar{\rho} \delta u'^{2}_{\parallel}} \Re\left(p'_l u'^{*}_{\parallel}\right) \quad (2)$$

with $\delta = 1 - f^2/\hat{\omega}^2$, a function of balloon latitude, and with f the inertial frequency and $\hat{\omega}$ the intrinsic frequency of the wave. Note here that the periods, momentum fluxes and phase speeds are in the intrinsic frame of the quasi-Lagrangian balloon observations.

In this study, we retain only the two largest amplitude wave packets at each time step (Figure 2). Although wave packets are only accounted for by their center, or maximum of amplitude, these two alone represent on average around 40% of the total momentum flux. In sensitivity tests, we compared moving mountain wave characteristics using only the first largest wave packet to the two-packet method, and the results were very similar, except the near-diurnal period was over emphasized, so we added the second wave packet. Note that the total momentum fluxes are computed in the direction of propagation of the waves. This was possible by making the assumption that all waves at the balloon levels propagate upwards (Vincent & Hertzog, 2014), which resolves a 180° direction ambiguity from the polarization relations. In this convention, the total fluxes are positive quantities. However, the zonal $(u'w')$ and meridional $(v'w')$ components, namely $u'_{\parallel} w'$ cos θ and $u'_{\parallel} w'$ sin θ respectively, are signed quantities.

The last step is to compute the ground-based phase speed. As in Vincent and Alexander (2000), it is the sum of the ground-based phase speed c with a projection of the wave propagation direction on the background flow:

$$c = \hat{c} + [\overline{u_b}, \overline{v_b}]. \frac{\vec{k}}{|\vec{k}|} \quad (3)$$

In the above equation, c is projected in the zonal and meridional direction with $[\overline{u_b}, \overline{v_b}]$ the daily mean horizontal flow at the balloon level.

For comparison to previous results, we show in Figure 3, the obtained distributions of density-weighted momentum flux (zonal and meridional) versus intrinsic and ground-based phase speeds, for the retrieved wave packets, as in Hertzog et al. (2008), for C0 campaign, as an example. The shape of the spectrum is similar to the Vorcore campaign results. Unlike Corcos et al. (2021), we find a significant difference at high momentum fluxes between the two flight levels. This can be explained by our focus here on the two largest amplitude wavepackets, that will be more easily dissipated between the TTL level (∼18 km) and the STR level (∼20 km). Indeed, previous observations of gravity wave momentum fluxes highlighted the importance of highly intermittent large amplitude wave events in the total momentum fluxes (Hertzog et al., 2012), which will tend to break at lower altitudes. These may be one of the key elements for realistic simulations of the stratospheric simulations and more precisely the QBO (Bushell et al., 2020; Vincent & Alexander, 2020). We find here a dissipation of ∼25% of the momentum flux between 18 and 20 km for the two campaigns.

Note also the possible change of ground-based phase speed sign for low intrinsic phase speeds that shifts the overall momentum fluxes distributions. Waves with a small ground-based phase speed carry either positive or negative momentum flux, depending on the background wind velocity.

Finally, depressurization events can occur when a superpressure balloon flies over an extremely cold convective cloud. During these events, the balloon behavior is not isopycnal anymore, and the observations were disregarded. In total they represented around 5% of our data set as in Corcos et al. (2021).

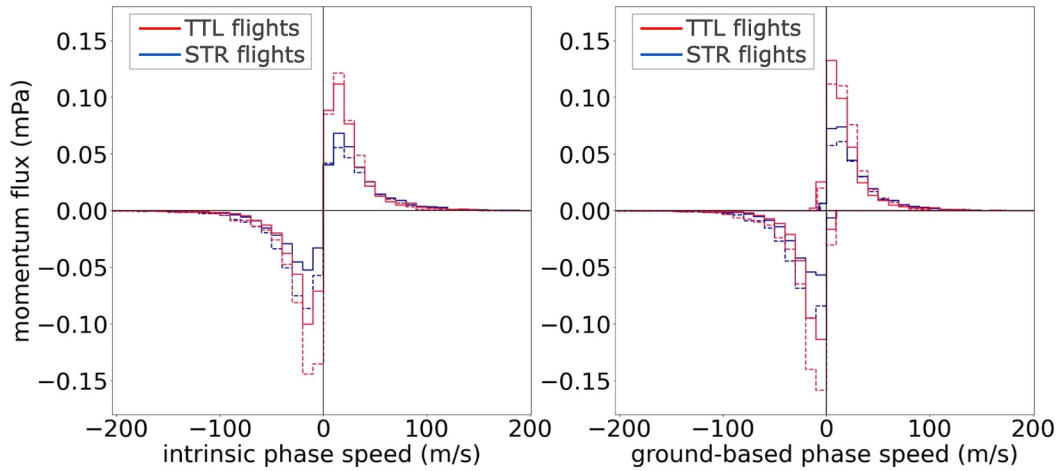

Figure 3. (left) Density-weighted zonal (full) and meridional (dashed) positive and negative bin-averaged momentum flux spectra of the retrieved wave packets versus the projection of the corresponding intrinsic phase speed on the zonal/meridional direction for tropical tropopause layer (red) and STR (blue) flights during C0. (right) As in the left panel, but for momentum fluxes and ground-based phase speed. C1 is not shown here.

2.3. Convective Environment and Identification of the Moving Mountain Waves

We used the Integrated Multi-satellitE Retrievals for GPM (IMERG) product to locate the Stratéole-2 balloons with respect to convective systems. IMERG for GPM gives a continuous precipitation data set since 2000, merging satellite radar-observations from Global Precipitation Measurement (GPM) and Tropical Rainfall Measuring Mission (TRMM) satellites with the constellation of infrared-observing weather satellites (Meteosat, Indoex, Himawari, GOES-W, and GOES-E) and using rain-gauge measurements for calibration (Huffman et al., 2019). This product is available at a half-hourly time resolution, and 0.1° × 0.1° spatial resolution. We define convective pixels as pixels with a rain rate higher than 5 mm/hr following Ryu et al. (2011). Figure 4 maps the IMERG convective rain pixels for C0 and C1 to show the overall patterns in rain during these two periods. We note the Indian Ocean Dipole (IOD) was in a positive phase during C0, and ENSO (El Niño-Southern Oscillation) was in the La Niña phase during C1.

IMERG for GPM convective rain pixels are co-located with each balloon position. Convective pixels are considered co-located if within each 1 hr-period they lie within a 300 km radius surrounding each balloon position based on Corcos et al. (2021) (their Figure 6). These co-located rain pixels are selected as significantly impacting the balloon observations of gravity waves and define the "convective environment" of the balloon observations. We find co-located convection at 40% and 44% of the time for C0 and C1, respectively, meaning that for around

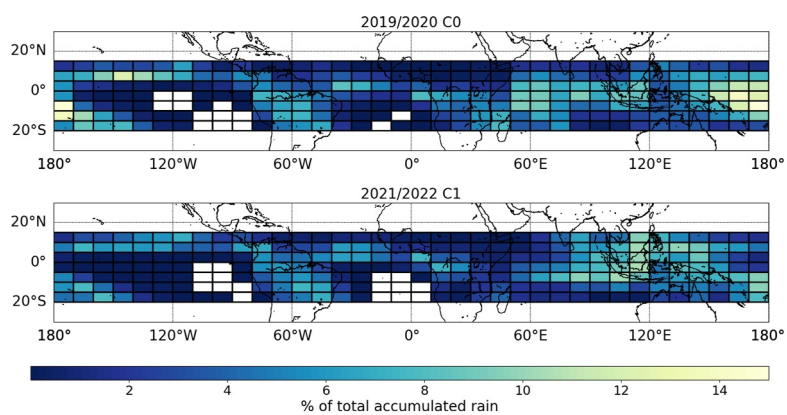

Figure 4. Maps of convective rain over the 20°S to 15°N latitudes covered in this study. Units are percent of total convective rain over the tropical band during the two campaign periods C0 (top) and C1 (bottom). Note: white boxes have no convective rain by our definition.

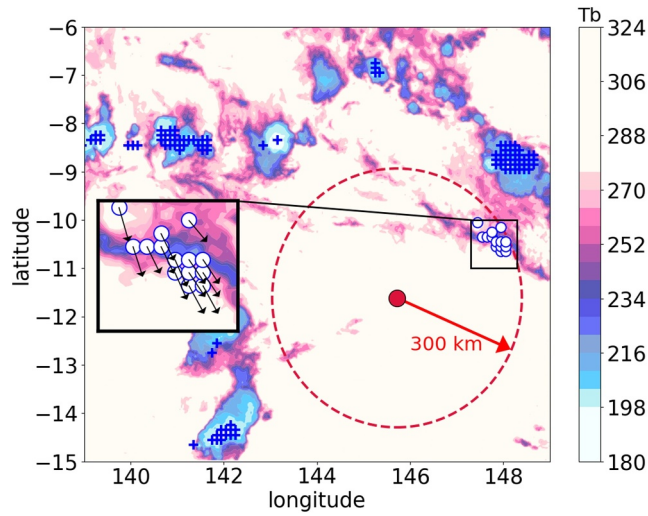

Figure 5. Illustration of the "co-location" method. Colors show a map of brightness temperature of the fifth of January, 10 UTC. Blue crosses correspond to pixels with a rain rate higher than 5 mm/hr, and white circles highlight those within a radius of 300 km (red dashed circle) around the balloon position (red dot). ERA5 700 hPa horizontal wind for the co-located convective rain pixels are represented with black arrows. Note that the IR brightness temperatures are used here to illustrate the environment and to derive convective pixel cloud top heights (see text).

half the time for both campaigns the balloons were positioned less than 300 km away from a raining convective cell.

At convective rain cell pixel positions, nearest neighbor ERA5 reanalysis profiles are identified. Cloud top height is calculated by interpolating the ERA5 geopotential height profile with ERA5 temperature profile and the global merged-IR brightness temperature within 0.036° of the rain pixel. Wind profiles at these points are also derived from ERA5.

In order to identify the waves generated by the moving mountain mechanism, we base our method on the formulation of Beres et al. (2004). The first step is to gather the co-located convective cell velocity and direction. Following Beres et al. (2005), we estimate the vector motion of each co-located rain cell as the wind at the steering level (700 hPa) from ERA5 profiles. We average those rain cell velocities and directions in the 300-km radius vicinity of the balloons for each hourly balloon position. Figure 5 illustrates the method, showing a Stratéole-2 balloon (red dot) on a background map of IR (InfraRed) brightness temperature. The IMERG convective pixels are marked as blue crosses, and those retained within the 300 km radius are overlain with white circles with a blue edge. Steering level winds for the co-located pixels are also shown with vectors. Note the similarity of the steering level wind directions within the convective complex in the vicinity of the balloon.

Next we predict the phase speed and direction of waves that would be generated by the moving mountain mechanism. According to Beres et al. (2004), such waves are stationary relative to the convective cell, so their ground-based phase speed is approximated by the cell speed identified in the previous paragraph. Theoretical propagation directions for moving mountain waves lie in the semi-circle of directions opposite to the vector wind at the top of the rain cell in the frame moving with the rain cell, "$\mathbf{u}_{rel}$." Figure 6 illustrates this wind and the direction criterion. The cell moves with the wind vector $\mathbf{u}_{700hPa}$ and the background wind vector at the top of the cell is labeled $\mathbf{u}$ and the moving mountain waves will propagate in the semi-circle of directions upstream of $\mathbf{u}_{rel}$, shaded green in the figure.

Finally, retrieved wave packets are identified as "moving mountain waves" at an hourly time resolution only if their ground-based phase speed is within the range $|\mathbf{u}_{700hPa}|\pm5$ m/s and if their direction lies within the green semi-circle. Both criteria must be met simultaneously for a wave packet to be identified with the moving mountain mechanism. Note that we tested the sensitivity of our results to a smaller angle opposite to $\mathbf{u}_{rel}$, using 90° instead of 180°, as well as to a larger ground-based phase speed range ±10 m/s, and this did not substantially change our results.

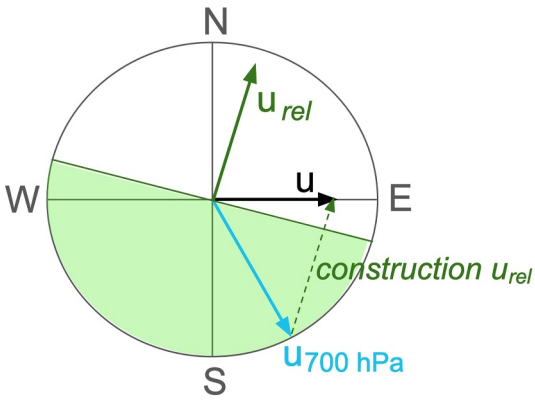

Figure 6. Example of zonal background wind at the top of the cell (black arrow) and south-east steering level wind (light blue) in polar representation. The average speed of convective cells with respect to the background wind (green arrow) defines the range of directions of propagation at its opposite (green half circle).

3. Results

3.1. Occurrence of the Moving Mountain Waves

Figure 7 presents the number of retrieved wave packets identified as from the moving mountain mechanism (hereafter called "moving mountain waves" or MM waves). Note the difference with Figure 1, which represented raw 30 s observations. Here, we illustrate hourly wave packets. Moving forward, all results will represent contributions of identified main pair of wave packets, at an hourly time resolution. For this figure, the small number of identified MM waves can be explained by close convection happening only half of the time, and criteria for MM waves only gathered 5% of the time when there is a convective cell in the right range. For better statistical robustness, we gathered wave packets at 18 and 20 km in this section.

Both campaigns show similar patterns with most MM waves above the Maritime Continent. This may be related to two different reasons: first, a stalling of the balloons above that region, especially in C1, and second its high convective activity. It is also interesting to describe the differences. First, the part of the Indian Ocean with the largest amount of observations seems to shift west from 2019 to 2021. This feature is explained by a positive event of the IOD that took place during C0, shifting the convection toward the west, and reducing overall the gradient of convection in the basin (Saji et al., 1999; Webster et al., 1999). The C1 campaign coincided with La Niña conditions, with more convective rain over the Maritime Continent (Figure 4). The second difference is the amount of MM wave observations above the Pacific Ocean during C0, which also mirrors the convective rain patterns.

3.2. Moving Mountain Waves Characteristics

We describe here qualitatively the wave packets from the moving mountain mechanism. Figure 8 displays distributions of wave periods observed during both campaigns. As mentioned, colocated observations, or observations with convective cell spotted in a 300 km radius around the balloons positions, represent half of the total observed data set, but the two distributions are similar. This is a good indicator of the uniformity of the subsampling due to the colocation process. This distribution highlights the prominence of smaller periods, up to 5 hr, and of the longer periods close to a day. The latter is partly affected by the balloon night/day oscillations that may have affected our results. We will come back to it in the next subsection. The distribution of wave packet periods for the MM waves (orange) highlights no preferential wave period associated with MM waves over the 2019/2020 campaign. In other words, the distribution of wave periods is similar to other CGWs, in line with Beres et al. (2004) simulations. Differences between the two campaigns might not be statistically significant. A slight

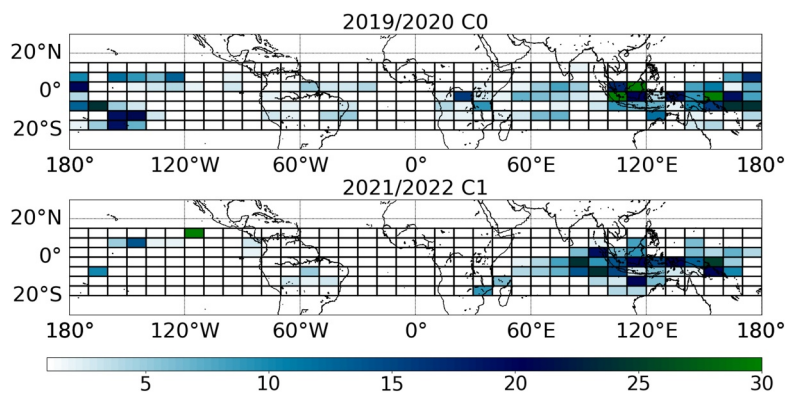

Figure 7. Number of retrieved wave packets identified as generated by the moving mountain mechanism, during the C0 campaign (upper panel) and C1 campaign (lower panel).

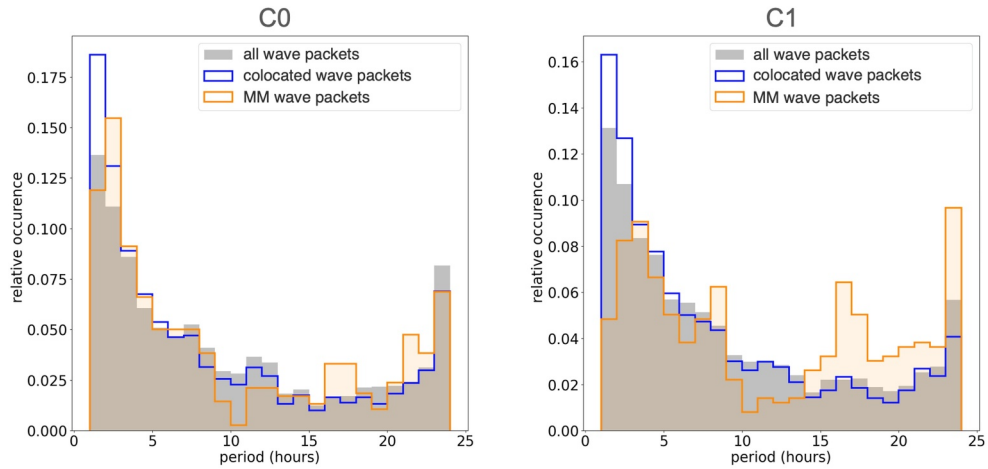

Figure 8. Distributions of identified wave packet intrinsic periods for 2019/2020 C0 and 2021/2022 C1 campaigns. The gray distribution shows the average from all hourly packets. The dark blue line is the distribution from packets collocated with Integrated Multi-satellitE Retrievals for GPM. The orange distribution corresponds to the MM wave packets. The relative occurrences are normalized such as the sum of the occurrences equals to one.

shift from shorter to longer wave periods with a higher peak near the diurnal cycle might be related to increased convection above the Maritime Continent in 2021/2022 (Figure 4) where there is a stronger diurnal cycle.

Figure 9 displays the horizontal wavelength distributions for the identified wave packets. The striking feature of this figure is the difference between the all-gravity-wave packets and the MM wave packet distribution (orange), as the latter shows a longer tail of shorter wavelengths. Thus, the average horizontal scale of the latter is reduced by 65%, from around 900 km (all colocated packets) to 300 km. This result is encouraging and in line with model studies (Clark et al., 1986). These waves are expected to occur with smaller scales, closer to the horizontal scale of the convective systems. It should also be noted that the apparent difference for all the packets between 2019 and 2021 is not significant: we choose the log-scale of the figure to highlight the smaller scales in the tail, whereas the mean horizontal wavelength only varies by 2% between the two campaigns.

3.3. Regional Variability: Land, Ocean, Maritime Continent

Corcos et al. (2021) and Wright et al. (2013) highlighted a difference between quieter oceanic regions and more active regions (continents and Maritime Continent), in agreement with Randel et al. (2021) and Ern and Preusse (2012). We thus distinguished three zones with different convective activity (Figure 10, upper panel):

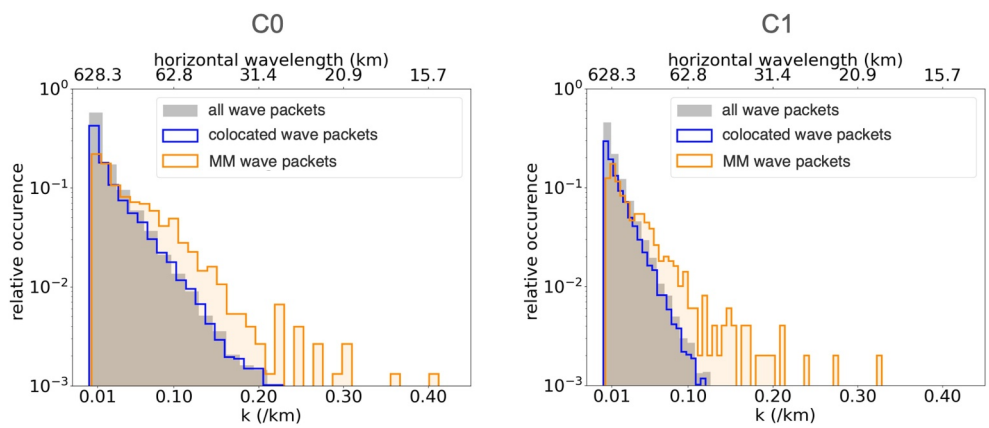

Figure 9. Distributions of horizontal wavelength and horizontal wave number for 2019/2020 C0 and 2021/2022 C1 campaigns. The gray distribution collects all hourly packets. The dark blue line is the distribution of packets collocated with Integrated Multi-satellitE Retrievals for GPM convection. The orange distribution corresponds to the wave packets identified as MM waves. The relative occurrences are normalized such as the sum of the occurrences equals to one.

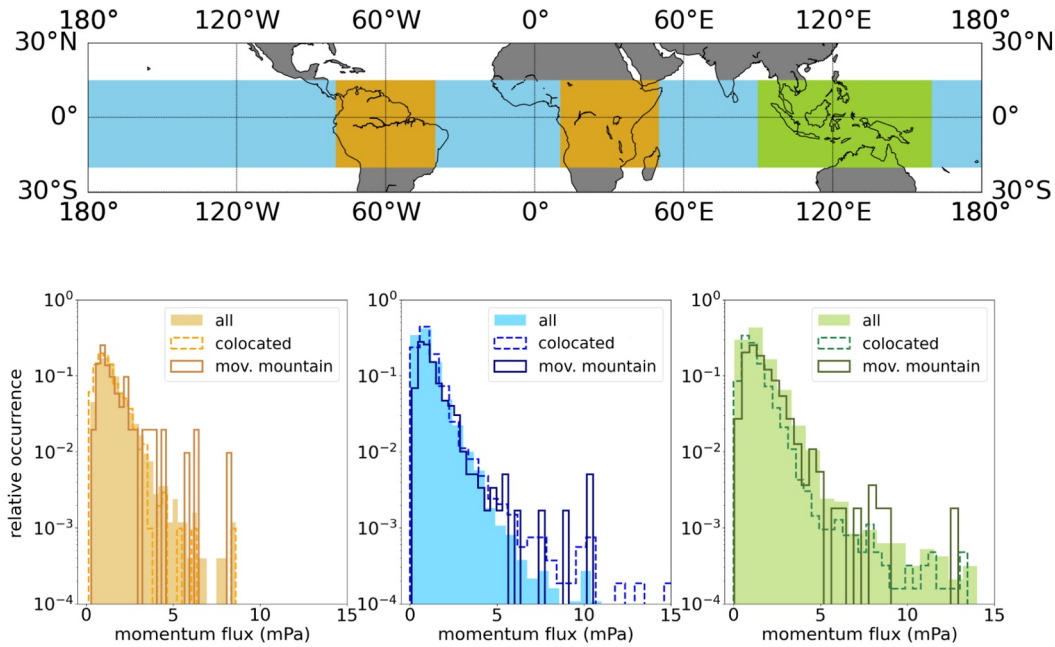

Figure 10. (Upper panel) Map of the continental (orange), oceanic (blue) and Maritime Continent (green) zones (Lower panel) Corresponding distributions of momentum fluxes, for all retrieved wave packets (filled), colocated retrieved wave packets (dashed line) and MM wave packets (solid line). The relative occurrences are normalized such as the sum of the occurrences equals to one.

continent, ocean, and Maritime Continent as balloons stalled in this region, giving particularly high sampling in 2021 (Figure 1). For more robust statistical results, we combined the two campaigns in this section. The overall retrieved wave packets show very similar average momentum flux above the continents and Maritime Continent, whereas flux is ∼30% smaller above the oceans (Table 2). This difference is expected, and further described in Figure 10 (lower panel): the Maritime Continent has a distribution with the longest tail of high momentum fluxes. This highlights the importance of a few larger events on the mean value. On the other hand, the tail of the flux distribution above the oceans decreases the fastest, with amplitudes above 5 mPa five to ten times less probable than elsewhere. The continental distribution exhibits an intermediate shape, with higher relative occurrence of momentum fluxes larger than 2 mPa compared to the oceans, but a shorter tail than the Maritime Continent.

The MM waves' distribution differs from the colocated wave packet distributions in the three zones, with a higher relative occurrence of larger events, resulting in an increase of the momentum flux average by 30% above the continents and Maritime Continent, and 40% above the oceans. Furthermore, Table 2 shows a shift in the relative occurrence of the MM waves in the three different regions, with the lowest relative occurrence above the Maritime Continent, and the highest above the oceans.

We also computed the intermittency of the gravity wave packets and the subset of MM waves, as the contribution of the highest 10% of fluxes in the distribution to the mean momentum flux (Alexander et al., 2010; Hertzog

Table 2
Statistical Results About the Computed Momentum Fluxes in the Three Different Regions Depicted in Figure 10

		Continents	Oceans	Maritime continent
All wave packets (colocated wave packets)	Mean flux/standard deviation (mPa)	1.3/0.8 (0.7/0.9)	0.9/0.7 (1.1/0.9)	1.2/0.9 (1.3/1.0)
	Intermittency (%)	24 (25)	28 (27)	26 (26)
Moving mountain mechanism	Mean flux/standard deviation (mPa)	1.7/1.4	1.3/1.1	1.7/1.2
	Intermittency (%)	30	29	25
	Occurrence (%)	5.0	5.5	4.7
	Contribution to the total flux (%)	7.0	6.7	5.5

et al., 2012; Plougonven et al., 2013). It describes further the distribution of momentum fluxes presented in Figure 10. Intermittency further quantifies the importance of the tails of the distributions in Figure 10. It is computed as:

$$\frac{\sum_{f_i > f_{q90}} f_i}{\sum_{i=1}^{N_{obs}} f_i} \times 100 \tag{4}$$

where f_i represents the instantaneous momentum flux from the two main wave packets, f_{q90} the momentum fluxes in the 90th quantile, N_{obs} the number of observation points. We find an overall intermittency of ∼27%, for both all retrieved wave packets and for the MM waves, in line with the values of Corcos et al. (2021) and Wright et al. (2013) for a spectrum of waves with periods from an hour to a day. The intermittency variability between the different convective zones is nonnegligible, in line with the shape of the distributions presented in Figure 10. This highlights the importance of a few larger events to the overall momentum flux, but this value is low compared to higher latitude regions where orographic waves are a more significant source of gravity waves (Hertzog et al., 2012; Jewtoukoff et al., 2015; Wright et al., 2013). Indeed, convective sources are intermittent but ubiquitous in the tropics, lowering the overall intermittency.

Finally, we examine the local-time variation of momentum flux of our colocated wave packets with convection. Figure 11 shows a clear diurnal cycle over land, with an increase of momentum flux amplitude, peaking in the late afternoon. The same diurnal cycle was observed for convection in many studies (Chaboureau et al., 2004; Hendon & Woodberry, 1993; Ohsawa et al., 2001; Yang & Slingo, 2001). The MM waves show the same diurnal cycle but even stronger, suggesting a strong relationship to the intense convection occurring in the late afternoon over land. The diurnal cycle over the oceans and the Maritime Continent in our data is not as clear, with only a slight increase of the oceanic fluxes at night, in line with convective and rain rate diurnal cycles as seen in TRMM (Collier & Bowman, 2004; Liu & Zipser, 2008).

Figure 11 lower panels also show the relative occurrence of retrieved wave packets at each hour of the day. It is additional information to understand the evolution of the observed momentum flux during the day. Unsurprisingly, the colocated observations show a uniform distribution of the observations within the day. This signal is more pronounced for the MM waves. It is possible that the diurnal cycle in colocated observations of both types could be in part an artifact from our method. We colocated the retrieved wave packets with convective pixels with a minimum rain rate of 5 mm/hr. These higher rain rates happen more preferentially in the mid afternoon, with a clearer signal above the continents than the oceans (Collier & Bowman, 2004; Negri et al., 2002). Therefore waves generated by these active cells will be more likely encountered during those times.

4. Discussion: Contribution to the QBO

The last step of our study is to quantify the contribution of the identified MM wave packets to the observed zonal momentum fluxes, and thus their contribution to the QBO. We decided to distinguish the two campaigns as they were during two slightly different phases of the QBO. During C0, the mean zonal wind at TTL and STR levels were ∼9 m/s and ∼2 m/s, respectively. During C1, these winds were ∼4.5 m/s and ∼2 m/s.

First, Figure 12 shows the spectrum of zonal momentum fluxes and ground-based phase speeds at 20 (left) and 18 km (right). Note the difference of momentum flux scale between the MM wave packets and colocated wave packets as the MM represent around 6% of the total flux in the colocated observations (see table 2). This figure highlights that the MM wave packets (lower panels) are concentrated in the low phase speeds, less than 15 m/s. Both colocated and MM retrieved wave packets show significant changes between the two balloon float levels during C0 (top row, blue). For C1 (green) the changes between the altitudes are comparatively small.

Table 3 presents the campaign average signed zonal wind tendencies due to dissipation of momentum flux between the two levels, computed as follows:

$$-\frac{1}{\bar{\rho}}\left(\frac{\sum_{STR}(\bar{\rho}_{STR}\overline{u'w'}_{STR})}{N_{STR}} - \frac{\sum_{TTL}(\bar{\rho}_{TTL}\overline{u'w'}_{TTL})}{N_{TTL}}\right) \tag{5}$$

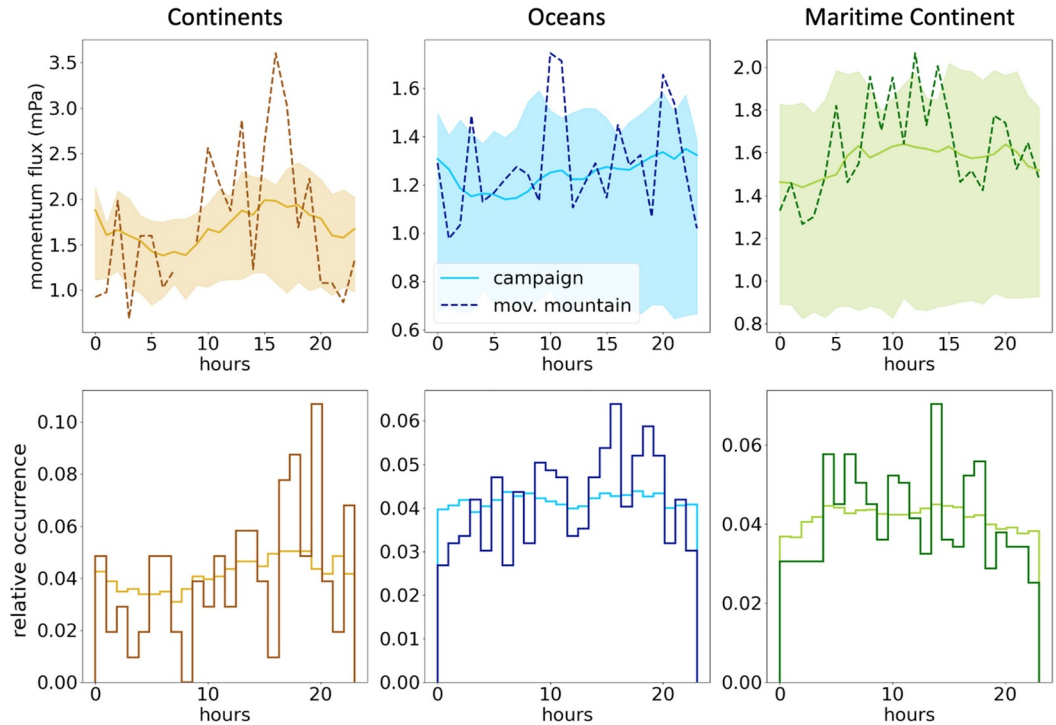

Figure 11. (Upper panel) Daily evolution of hourly averaged momentum fluxes in the continental (orange), oceanic (blue) and Maritime Continent (green) zones. Full and dashed lines are respectively the average of all colocated wave packets and average of the MM waves. The upper and lower boundaries of the color field area represent the first and third quartiles of the colocated wave packets (Lower panel) Corresponding relative occurrence of wave packets colocated with convection. In all panels the lighter colors represent all colocated wave packets and the darker colors represent the MM detections only. The relative occurrences are normalized such as the sum of the occurrences equals to one.

with $\bar{\rho}$ the averaged density between 18 and 20 km, N_{TTL} and N_{STR} the number of retrieved wave packets at 18 and 20 km. The zonal tendencies associated with the MM waves is stronger in C0 than C1. We hypothesize that the weak MM momentum fluxes and zonal tendencies during C1 are mainly related to the weaker winds and shear, such that these low phase speed waves have previously dissipated below the TTL level. We also note that future observations, planned in 2025 for the next phase of Stratéole-2 will be valuable because of the potential influences of sampling differences in these results.

In terms of contributions to the QBO forcing, C0 and C1 were during the eastward phase, where C1 was closer to the transition phase. Therefore, background wind shear was negative during both campaigns but weaker in the second one (respectively −3.4 m/s/km and −1.3 m/s/km based on the balloon in situ observations).

The forcing needed to drive the QBO is not constant with height, but is much smaller (in terms of m/s/day) in the lowermost stratosphere (e.g., Alexander and Ortland (2010); Pahlavan et al. (2021)). At the balloons levels, it is about 0.3–0.4 m/s/day. All net zonal tendencies are negative, for C0 and C1, as expected in these negative shear conditions. We find that the waves of the colocated observations are counting up to 60% of the drive required for this phase of the QBO during C1. Note that these results are based on our primary focus on large amplitude waves and lower phase speeds that are assumed to drive the QBO at lower altitudes. These waves are rarely with periods smaller than 1 hr, thus, waves with periods down to 15 min, which contribute to the total momentum flux (Corcos et al., 2021), should not change the sign of the net zonal momentum tendency found here.

In addition, the contribution of the MM waves is not negligible, with a negative net tendency in both campaigns. During C0, the MM wave net tendency is even larger than the net tendency associated with all the colocated waves, suggesting that these MM waves can have an outsized effect on the QBO below 20 km considering their relatively rare occurrence and relatively small contribution to the total gravity wave momentum fluxes (Table 2). Finally, note that the noise floor for momentum flux is $\sim 10^{-4}$ mPa (Vincent & Hertzog, 2014). Thus, zonal

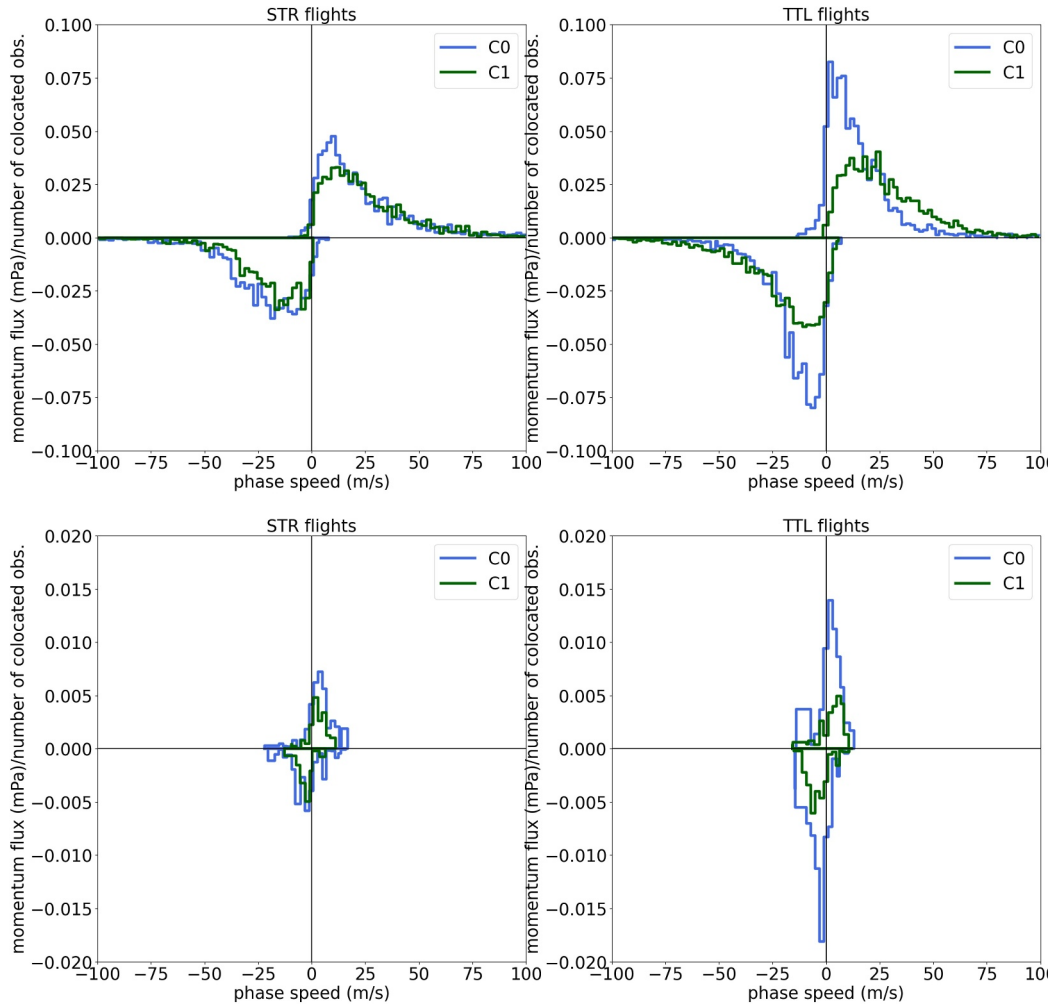

Figure 12. (Upper panels) Distributions of zonal momentum fluxes as a function of ground-based phase speeds for the colocated wave packets of both campaigns, at 20 (left) and 18 km (right), within 10° of the equator. (Lower panels) Same but only for the identified MM wave packets. The distributions are normalized such that the integrated positive and negative momentum fluxes equal the zonal-mean positive and negative values, respectively.

momentum tendency uncertainties can be estimated as $10^{-4}\sqrt{2}/\rho$, ~0.0014, which is order of magnitude smaller than the net tendency computed here.

Table 3
Wind Tendencies Between 18 and 20 km Averaged Over ±10° Latitudes

		Zonal momentum tendency (m/s/day)		
		Positive	Negative	Net
Colocated observations	C0	0.27	−0.29	−0.02
	C1	0.14	−0.31	−0.17
Moving mountain mechanism	C0	0.03	−0.06	−0.03
	C1	0.01	−0.02	−0.01

5. Summary and Conclusions

We presented observations of convective gravity waves in the tropical band from Stratéole-2 superpressure balloons. These observations gather two campaigns, C0 in 2019–2020 and C1 in 2021–2022, with a total number of 24 balloons, that flew at 18 and 20 km of altitude up to several months each. We presented gravity wave packets intrinsic and ground-based phase speeds as well as momentum fluxes. We followed the description of waves generated by the moving mountain mechanism described in Beres et al. (2004) in order to identify them in our data set of retrieved wave packets. We first hourly colocated the balloons with convective cells in a 300 km vicinity, tracking the direction of propagation of the cells using the ERA5 wind at 700 hPa. The "moving mountain waves" have a ground-based phase speed near the speed of propagation of the convective cells. These waves have an average horizontal

wavelength of ∼300 km and a distribution of wave periods similar to other convective gravity wave packets. They occur only ∼5% of the time but contribute up to ∼7% of the total observed flux, with a maximum above the continents.

In terms of contribution to the QBO forcing, we described the dissipation of the observed gravity waves between 18 and 20 km. We find a higher dissipation of the smaller ground-based phase speed (up to 25 m/s) waves during the 2019–2020 campaign, that took place during an eastward phase of the QBO. The 2021–2022 campaign happened closer to the transition phase, with a weakening of the wind shear of around 66%. Overall, we find that the convective gravity wave packets are responsible for up to 2/3 of the required force to drive the QBO at these low altitudes. Finally, "moving mountain waves" have a stronger dissipation between 18 and 20 km than the average retrieved wave packet. Therefore, even with an overall small contribution to the observed flux, they are responsible for up to 10% of the required drive for the QBO. Given that the MM waves dissipate mostly in the lowermost stratosphere, they play an important role for the QBO to propagate to these low levels.

Data Availability Statement

Strateole-2 data are available on https://data.ipsl.fr/catalog/strateole2/ and thredds-x.ipsl.fr/thredds/catalog/C1/catalog.html. Integrated Multi-satellitE Retrievals for GPM is available at Huffman et al. (2019).

Acknowledgments
The Tsen data were collected as part of Strateole-2, which is sponsored by CNES, CNRS/INSU, and NSF. Joan Alexander, Martina Bramberger, and Milena Corcos were supported by NSF Grants 2231667 and 2110002. The authors would like to acknowledge Agustin Caro, the LATMOS gondola team, and Karim Ramage for their expertise and patience in the field. We give special thanks to Stephanie Venel and the CNES ballooning team for their exceptional balloon launches, professionalism, and for making these difficult measurements possible.

References

Alexander, M. J., Geller, M., McLandress, C., Polavarapu, S., Preusse, P., Sassi, F., et al. (2010). Recent developments in gravity-wave effects in climate models and the global distribution of gravity-wave momentum flux from observations and models. *The Quarterly Journal of the Royal Meteorological Society*, *136*(650), 1103–1124. https://doi.org/10.1002/qj.637

Alexander, M. J., Liu, C. C., Bacmeister, J., Bramberger, M., Hertzog, A., & Richter, J. H. (2021). Observational validation of parameterized gravity waves from tropical convection in the whole atmosphere community climate model. *Journal of Geophysical Research*, *126*(7). https://doi.org/10.1029/2020jd033954

Alexander, M. J., & Ortland, D. A. (2010). Equatorial waves in High Resolution Dynamics Limb Sounder (HIRDLS) data. *Journal of Geophysical Research*, *115*(D24). https://doi.org/10.1029/2010jd014782

Alexander, M. J., Richter, J. H., & Sutherland, B. R. (2006). Generation and trapping of gravity waves from convection with comparison to parameterization. *Journal of the Atmospheric Sciences*, *63*(11), 2963–2977. https://doi.org/10.1175/jas3792.1

Anstey, J., Osprey, S. M., Alexander, M. J., Baldwin, M., Butchart, N., Gray, L., et al. (2022). Impacts, processes and projections of the quasi-biennial oscillation. *Nature Reviews Earth & Environment*, *3*(3), 588–603. https://doi.org/10.1038/s43017-022-00323-7

Baldwin, M. P., Gray, L. J., Dunkerton, T. J., Hamilton, K., Haynes, P. H., Randel, W. J., et al. (2001). The quasi-biennial oscillation. *Review of Geophysics*, *39*(2), 179–229. https://doi.org/10.1029/1999RG000073

Beres, J. H., Alexander, M. J., & Holton, J. R. (2004). A method of specifying the gravity wave spectrum above convection based on latent heating properties and background wind. *Journal of the Atmospheric Sciences*, *61*(3). https://doi.org/10.1175/1520-0469(2004)061⟨0324:AMOSTG⟩2.0.CO;2

Beres, J. H., Garcia, R. R., Boville, B. A., & Sassi, F. (2005). Implementation of a gravity wave source spectrum parameterization dependent on the properties of convection in the whole atmosphere community climate model (WACCM). *Journal of Geophysical Research*, *110*(D10). https://doi.org/10.1029/2004jd005504

Boccara, G., Hertzog, A., Vincent, R. A., & Vial, F. (2008). Estimation of gravity wave momentum flux and phase speeds from quasi-Lagrangian stratospheric balloon flights. Part I: Theory and simulations. *Journal of the Atmospheric Sciences*, *65*(10), 3042–3055. https://doi.org/10.1175/2008JAS2709.1

Bramberger, M., Alexander, M. J., Davis, S., Podglajen, A., Hertzog, A., Kalnajs, L., et al. (2022). First super-pressure balloon-borne fine-vertical-scale profiles in the upper TTL: Impacts of atmospheric waves on cirrus clouds and the QBO. *Geophysical Research Letters*, *49*(5). https://doi.org/10.1029/2021gl097596

Bushell, A. C., Anstey, J. A., Butchart, N., Kawatani, Y., Osprey, S. M., Richter, J. H., et al. (2020). Evaluation of the quasi-biennial oscillation in global climate models for the sparc qbo-initiative. *Quarterly Journal of the Royal Meteorological Society*, *148*(744), 1459–1489. https://doi.org/10.1002/qj.3765

Chaboureau, J., Guichard, F., Redelsperger, J., & Lafore, J. (2004). The role of stability and moisture in the diurnal cycle of convection over land. *The Quarterly Journal of the Royal Meteorological Society*, *130*(604), 3105–3117. https://doi.org/10.1256/qj.03.132

Clark, T. L., Hauf, T., & Kuettner, J. P. (1986). Convectively forced internal gravity waves: Results from two-dimensional numerical experiments. *The Quarterly Journal of the Royal Meteorological Society*, *112*(474), 899–925. https://doi.org/10.1002/qj.49711247402

Collier, J. C., & Bowman, K. P. (2004). Diurnal cycle of tropical precipitation in a general circulation model. *Journal of Geophysical Research*, *109*(D17). https://doi.org/10.1029/2004jd004818

Corcos, M., Hertzog, A., Plougonven, R., & Podglajen, A. (2021). Observation of gravity waves at the tropical tropopause using superpressure balloons. *Journal of Geophysical Research*, *126*(15). https://doi.org/10.1029/2021jd035165

Ern, M., & Preusse, P. (2012). Gravity wave momentum flux spectra observed from satellite in the summertime subtropics: Implications for global modeling. *Geophysical Research Letters*, *39*(15). https://doi.org/10.1029/2012gl052659

Fritts, D. C., & Alexander, M. J. (2003). Gravity wave dynamics and effects in the middle atmosphere. *Review of Geophysics*, *41*(1). 3-1–3-64. https://doi.org/10.1029/2001RG000106

Hendon, H. H., & Woodberry, K. (1993). The diurnal cycle of tropical convection. *Journal of Geophysical Research*, *98*(D9), 16623–16637. https://doi.org/10.1029/93jd00525

Hertzog, A., Alexander, M. J., & Plougonven, R. (2012). On the intermittency of gravity wave momentum flux in the stratosphere. *Journal of the Atmospheric Sciences*, *69*(11), 3433–3448. https://doi.org/10.1175/JAS-D-12-09.1

Hertzog, A., Boccara, G., Vincent, R. A., Vial, F., & Cocquerez, P. (2008). Estimation of gravity wave momentum flux and phase speeds from quasi-Lagrangian stratospheric balloon flights. Part II: Results from the Vorcore campaign in Antarctica. *Journal of the Atmospheric Sciences*, *65*(10), 3056–3070. https://doi.org/10.1175/2008JAS2710.1

Huffman, G., Stocker, E., Bolvin, D., Nelkin, E., & Tan, J. (2019). GPM IMERG final precipitation L3 half hourly 0.1 degree x 0.1 degree V06 [Dataset]. Goddard Earth Sciences Data and Information Services Center (GES DISC). https://doi.org/10.5067/GPM/IMERG/3B-HH/07. Accessed 1 Aug 2023.

Jewtoukoff, V., Hertzog, A., Plougonven, R., de la Cámara, A., & Lott, F. (2015). Comparison of gravity waves in the southern hemisphere derived from balloon observations and the ECMWF analyses. *Journal of the Atmospheric Sciences*, *72*(9), 3449–3468. https://doi.org/10.1175/jas-d-14-0324.1

Liu, C., & Zipser, E. J. (2008). Diurnal cycles of precipitation, clouds, and lightning in the tropics from 9 years of trmm observations. *Geophysical Research Letters*, *35*(4). https://doi.org/10.1029/2007gl032437

Negri, A. J., Bell, T. L., & Xu, L. (2002). Sampling of the diurnal cycle of precipitation using trmm. *Journal of Atmospheric and Oceanic Technology*, *19*(9). https://doi.org/10.1175/1520-0426(2002)019⟨1333:SOTDCO⟩2.0.CO;2

Ohsawa, T., Ueda, H., Hayashi, T., Watanabe, A., & Matsumoto, J. (2001). Diurnal variations of convective activity and rainfall in tropical asia. *Journal of Meteorological Society of Japan. Series II*, *79*(1B), 333–352. https://doi.org/10.2151/jmsj.79.333

Pahlavan, H. A., Wallace, J. M., Fu, Q., & Kiladis, G. N. (2021). Revisiting the quasi-biennial oscillation as seen in ERA5. Part II: Evaluation of waves and wave forcing. *Journal of the Atmospheric Sciences*, *78*(3), 693–707. https://doi.org/10.1175/jas-d-20-0249.1

Pfister, L., Scott, S., Loewenstein, M., Bowen, S., & Legg, M. (1993). Mesoscale disturbances in the tropical stratosphere excited by convection: Observations and effects on the stratospheric momentum budget. *Journal of the Atmospheric Sciences*, *50*, 1058–1075. https://doi.org/10.1175/1520-0469(1993)050⟨1058:MDITTS⟩2.0.CO;2

Plougonven, R., Hertzog, A., & Guez, L. (2013). Gravity waves over Antarctica and the southern ocean: Consistent momentum fluxes in mesoscale simulations and stratospheric balloon observations. *Quarterly Journal of the Royal Meteorological Society*, *139*(670), 101–118. https://doi.org/10.1002/qj.1965

Podglajen, A., Hertzog, A., Plougonven, R., & Legras, B. (2016). Lagrangian temperature and vertical velocity fluctuations due to gravity waves in the lower stratosphere. *Geophysical Research Letters*, *43*(7), 3543–3553. https://doi.org/10.1002/2016GL068148

Podglajen, A., Hertzog, A., Plougonven, R., & Žagar, N. (2014). Assessment of the accuracy of (re)analyses in the equatorial lower stratosphere. *Journal of Geophysical Research*, *119*(19), 166–188. https://doi.org/10.1002/2014JD021849

Randel, W. J., Wu, F., & Podglajen, A. (2021). Equatorial waves, diurnal tides and small-scale thermal variability in the tropical lower stratosphere from COSMIC-2 radio occultation. *Journal of Geophysical Research*, *126*(7). https://doi.org/10.1029/2020jd033969

Richter, J. H., Sassi, F., & Garcia, R. R. (2010). Toward a physically based gravity wave source parameterization in a general circulation model. *Journal of the Atmospheric Sciences*, *67*(1), 136–156. https://doi.org/10.1175/2009jas3112.1

Ryu, J.-H., Alexander, M. J., & Ortland, D. A. (2011). Equatorial waves in the upper troposphere and lower stratosphere forced by latent heating estimated from trmm rain rates. *Journal of the Atmospheric Sciences*, *68*(10), 2321–2342. https://doi.org/10.1175/2011JAS3647.1

Saji, N. H., Goswami, B. N., Vinayachandran, P. N., & Yamagata, T. (1999). A dipole mode in the tropical Indian Ocean. *Nature*, *401*(6751), 360–363. https://doi.org/10.1038/43854

Stockwell, R., Mansinha, L., & Lowe, R. (1996). Localization of the complex spectrum: The s transform. *IEEE Transactions on Signal Processing*, *44*(4), 998–1001. https://doi.org/10.1109/78.492555

Vincent, R. A., & Alexander, M. J. (2000). Gravity waves in the tropical lower stratosphere: An observational study of seasonal and interannual variability. *Journal of Geophysical Research*, *105*(D14), 17971–17982. https://doi.org/10.1029/2000jd900196

Vincent, R. A., & Alexander, M. J. (2020). Observational studies of short vertical wavelength gravity waves and interaction with QBO winds. *Journal of Geophysical Research*, *27*. https://doi.org/10.1029/2020JD032779

Vincent, R. A., & Hertzog, A. (2014). The response of superpressure balloons to gravity wave motions. *Atmospheric Measurement Techniques*, *7*(4), 1043–1055. https://doi.org/10.5194/amt-7-1043-2014

Webster, P. J., Moore, A. M., Loschnigg, J. P., & Leben, R. R. (1999). Coupled ocean–atmosphere dynamics in the indian ocean during 1997–98. *Nature*, *401*(6751), 356–360. https://doi.org/10.1038/43848

Wright, C. J., Osprey, S. M., & Gille, J. C. (2013). Global observations of gravity wave intermittency and its impact on the observed momentum flux morphology. *Journal of Geophysical Research*, *118*(19), 10980–10993. https://doi.org/10.1002/jgrd.50869

Yang, G.-Y., & Slingo, J. (2001). The diurnal cycle in the tropics. *Monthly Weather Review*, *129*(4). https://doi.org/10.1175/1520-0493(2001)129⟨0784:TDCITT⟩2.0.CO;2